PROCEEDINGS, 49th Workshop on Geothermal Reservoir Engineering
Stanford University, Stanford, California, February 12-14, 2024
SGP-TR-227

Factors Controlling Rate and Magnitude of Seismicity Induced by Geothermal Well Stimulation

Taeho Kim and Jean-Philippe Avouac

1200 E. California Blvd., Pasadena, CA 91125

tkim5@caltech.edu , avouac@caltech.edu

Keywords: Induced Seismicity. Computational Modeling.

ABSTRACT

Advancements central to the world's transition to a greener economy such as geothermal energy are hampered by a lack of understanding and control of the maximum magnitude event. We develop a physical model for induced seismicity rate and identify the dominant factors on induced event magnitudes from the data. Induced seismicity observed during Enhanced Geothermal Stimulation (EGS) at Otaniemi, Finland and the Basel Deep Heat Mining project are reproduced by a physical model based on pore pressure diffusion and rate-and-state friction. The physical models produce simulations closest to the observations when assuming rate-and-state friction for shear failure with a diffusivity matching the pressure build-up at the well-head at onset of injections. At the same time, pressure drawdown immediately following shut-ins is best modeled with a lower diffusivity, indicating a significant change in diffusivity through fracture opening and closure. Seismicity rate following shut-in in Basel also indicates slower diffusion mechanisms. The potential of the model to serve as a forecasting tool is demonstrated by a pseudo-forecast that closely matches the entire seismicity rate history, using only the first injection stage as the training period. Next, we focus on the magnitude-frequency distribution of seismicity and how they may correlate to the injections. We observe a dominant, negative correlation of the *b*-value and maximum magnitude to depth in Otaniemi, although we do not observe the same relationship in Basel. Following a correction of the magnitudes to de-trend the dependence on depth in Otaniemi, both catalogs show a positive correlation between maximum magnitude and cumulative injected volume. We also observe a similar non-linear relationship between the magnitude-frequency distribution and distance from the injection source for the two catalogs. The identification of factors controlling seismicity rate and magnitudes provides basis for a control and optimization framework that may be utilized for sophisticated design of injection schedules.

1. INTRODUCTION

It has long been known that injection of fluids in the subsurface can induce seismicity (e.g., Healy et al., 1968; Raleigh et al., 1976; Aki et al., 1982). This issue has been put in the spotlight in recent years due to spikes of induced seismicity in regions with previously low levels of risk from earthquakes (Elsworth et al., 2016). While induced seismicity has been linked primarily to hydraulic fracturing for natural gas or `fracking', it is also a concern in the context of geothermal energy production (Gaucher et al., 2015; Majer et al., 2007; Zang et al., 2014). Induced seismicity is an undesirable by-product of this process, and a number of Enhanced Geothermal Systems (EGS) has been stopped due to earthquakes felt by local residents (Häring et al., 2008; Kwiatek et al., 2019; Schultz et al., 2020). The development of Enhanced Geothermal Systems (EGS) would therefore benefit from better methods to forecast injection-induced seismicity, and in particular, the earthquake magnitudes.

Numerous physical models have been developed to incorporate stress changes, pore-pressure changes and failure mechanisms in a single framework (Gaucher et al., 2015; Grigoli et al., 2017) to forecast induced seismicity. A notable example of physical models is presented by Segall & Lu (2015), where changes in stresses by fluid injections into an infinite poro-elastic medium were used as input to the model of Dieterich (1994), relating seismicity and stress rates among a population of nucleation sources. The framework has since then been used to study induced seismicity in response to various injection scenarios (e.g., Kim & Avouac, 2023; Zhai & Shirzaei, 2018).

In terms of earthquake magnitude, both natural and induced seismicity have been observed to follow the Gutenberg-Richter law, an empirical power law distribution with a shape parameter *b* that represents the proportion of large to small events (for a fixed number of total events, lower *b*-value translates to higher chances of large events). The number of events, *N*, larger or equal to magnitude *M* follows:

$$log_{10}N(\geq M) = a_{gr} - bM$$

where a_{gr} is an additional parameter to match to the total number of events. Although it is widely accepted that the Gutenberg-Richter law stems from heterogeneities (e.g., of fault sizes, rheological and frictional properties, stress distributions, etc.), whether seismologically observable variables such as the average stress state or local perturbation rates significantly influence or even control the *b*-value remains an open question. Two of the more widely cited correlations of the *b*-value to physical variables are to depth (Mori and Abercrombie, 1997; Spada et al., 2013) and focal mechanisms (Gulia & Wiemer, 2010; Schorlemmer et al., 2005) which can be jointly re-interpreted as a negative correlation to differential stress (Scholz, 2015). More specifically with respect to injection induced seismicity, the maximum magnitude, M_{max}, has been related to the cumulative injected volume, V_{max}, by assuming completely seismic release of all elastic energy stored by fluid injections through a group of events with a static *b*-value (McGarr, 2014). Alternatively, it has also been proposed that

M_{max} at various fluid injection sites are statistically consistent with the Gutenberg-Richter distribution observed under tectonic settings, with loading from injections replacing tectonic loading (van der Elst et al., 2016).

In this study, we apply physical models of injection-induced seismicity rate to two separate geothermal stimulation operations: 1. the 2018 Otaniemi EGS (Hillers et al., 2020; Kwiatek et al, 2019; Leonhardt et al., 2021) and the Basel Deep Heat Mining project (Häring et al., 2008). In the case of Otaniemi, we demonstrate the potential of the model to serve as a forecasting tool, by performing a pseudo-forecast of the observed seismicity rate. We also discuss possible quantitative inconsistencies between the intended physical meaning of model parameters and their inferred values. Finally, we analyze the magnitude-frequency distributions of both catalogs, and compare them to previously observed trends in both natural and induced seismicity.

2. CATALOGS AND INJECTION SCHEDULES

Both the earthquake catalogs and injection schedules of the Basel and Otaniemi stimulations are retrieved from publicly available databases, described in detail by Herrmann, et al. (2019) and Leonhardt, et al. (2021), respectively. The catalogs consist of approximately 280,000 events over a course of 10 days for Basel and 60,000 events over 50 days for Otaniemi. The hourly seismicity rates in Otaniemi are shown in Figure 1 along with the injection rate. Partial portions of the catalogs are relocated for improved spatial resolution, with 1,982 relocated events in Basel and 1,986 relocated events for Otaniemi. The relocated catalogs in their radial distribution with time are shown in Figure 2.

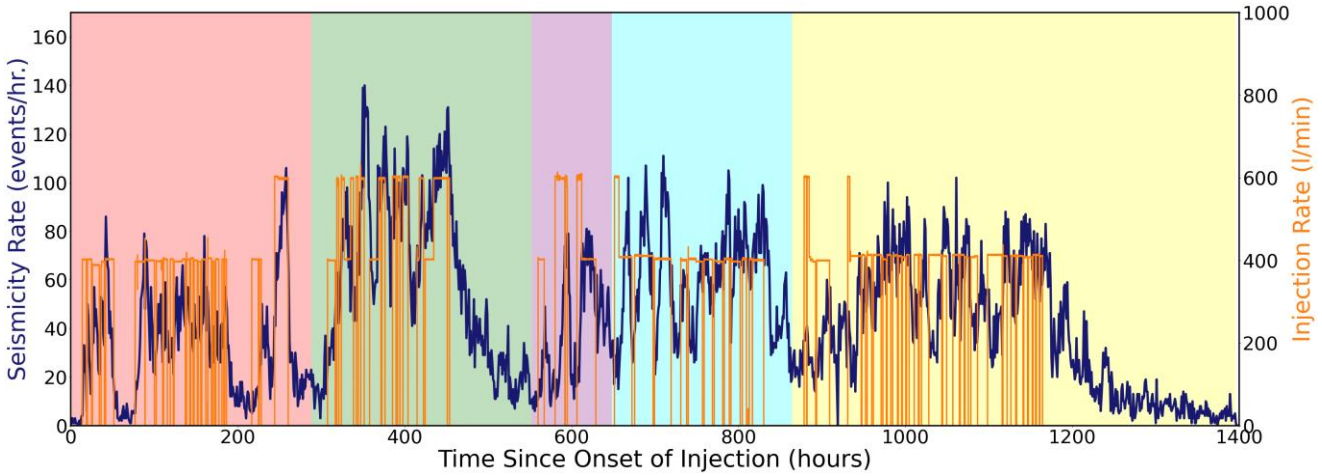

Figure 1: Earthquake Catalog in Otaniemi: The hourly seismicity rate of the complete catalog of Leonhardt et al. (2021) is plotted in dark blue. The injection rate is plotted in orange. The background colors represent the timing of the individual injection stages. The seismicity rate shows a positive correlation to the injection rate.

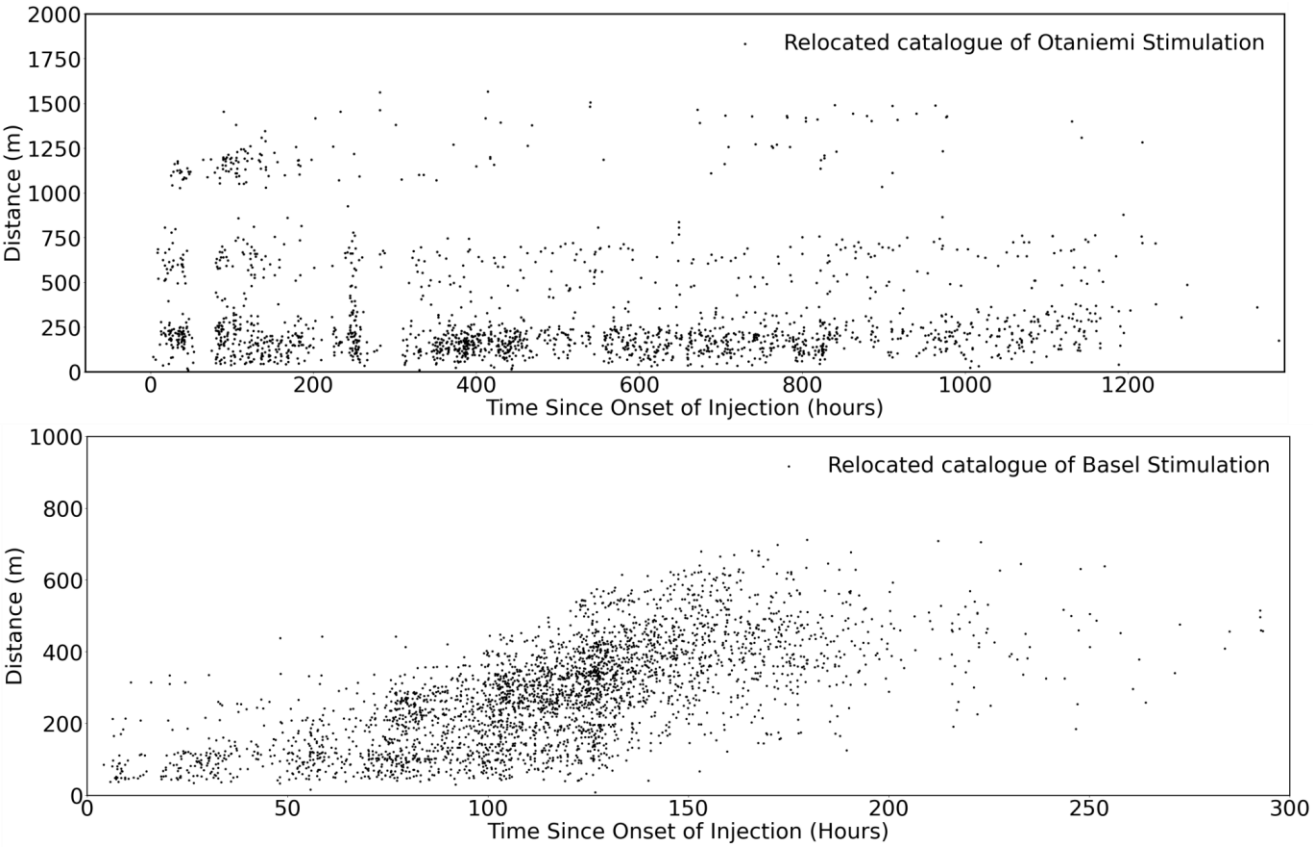

Figure 2: Relocated Catalogs of Otaniemi and Basel: Events with improved spatial resolution are plotted in their radial distance away from the injection source. In the case of Otaniemi where the injection location varied between different stages, the events are plotted with respect to the first injection source.

2.1 Sensitivity of seismicity rate to magnitude of completeness in Basel

The large sample size of the Basel catalog allows distinguishing features of the seismicity rate history with respect to the magnitude of completeness. Although the magnitude of completeness was estimated to be around -0.15 in Basel, the seismicity rate shows a systematic trend in its sensitivity to injection rate changes down to a magnitude of completeness of -1.0. Figure 3 compares the seismicity rate histories for M_c of -1.0, -0.5, and 0. The immediate seismic response to injection rate changes is heightened at lower M_c's. A gradual decay of the seismicity rate since the peak at a sudden change in the injection rate is therefore visible at lower M_c's, while higher M_c's show no systematic evolution. Such features indicate a possible dependence of earthquake nucleation on available energy at each nucleation source. The differences in seismicity rate histories would also lead to the inference of different physical parameters when matching the catalogs with a physical model.

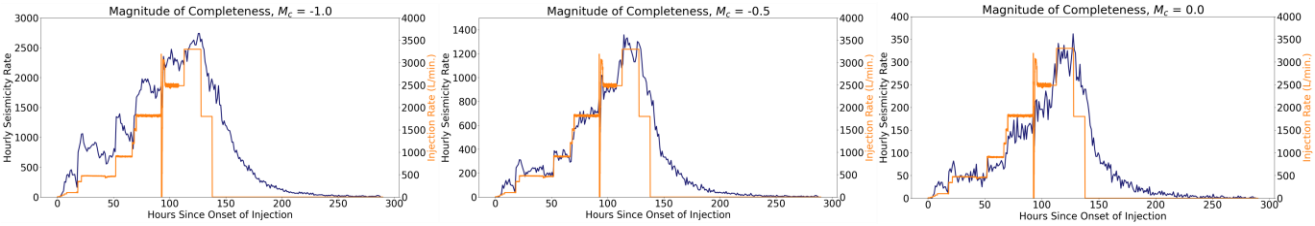

Figure 3: Earthquake Catalog in Basel at Different Magnitudes of Completeness: The hourly seismicity rate of the complete catalog of Herrmann et al. (2019) is plotted in dark blue, and the injection rate is plotted in orange. The seismicity rate in Basel shows higher peaks in response to rapid changes in the injection rate at lower magnitudes of completeness.

3. PHYSICAL MODELING OF FLUID DIFFUSION AND SEISMICITY RATE

Induced seismicity can result from either a stress or strength change on a fracture or fault. The effect of injection is generally assessed by considering pore pressure diffusion in the medium and the consequent decrease in the effective normal stress as according to Terzaghi's principle (Skempton, 1984). This first-order description of the stress state has been effective in explaining various aspects of induced seismicity, including the evolution of the seismicity front in space (Shapiro et al., 1997, 2006) and general spatiotemporal patterns of induced seismicity (Elmar & Shapiro, 2002; Shapiro et al., 1999, 2002) as early as the pioneering study at the Rangely oil field (Raleigh et al., 1976). The pressure increase can result in shear fractures (Mode-II or Mode-III), that under instability slip seismically as earthquakes. There is ample evidence from laboratory studies and natural observations that the initiation of slip involves a gradual decrease of friction associated with asesimic slip, often referred to as the nucleation process. Such an evolution of friction is commonly described

using the rate-and-state friction law derived from frictional sliding experiments in the laboratory (Dieterich, 1994; Dieterich & Linker, 1992; Marone, 1998; Ruina, 1983).

The physical model is based on stress evolution from pore pressure diffusion along with shear failure criterion following rate-and-state friction. The medium is treated to be infinite, homogeneous and isotropic. Neglecting the effect of the free surface is justified by the relatively large depths of the injections (4 – 6km) compared to the dimensions of the seismicity cloud (Figure 2). The induced stresses can then be calculated using the analytical solutions for a point source from Rudnicki (1986):

$$p(r,t) = \frac{q}{4\pi\rho r}\frac{\eta}{k} erfc\left(\frac{\xi}{2}\right)$$

$$\xi = \frac{r}{\sqrt{ct}}$$

$$c = \frac{k}{\eta}\frac{(\lambda_u - \lambda)(\lambda + 2\mu)}{\alpha^2(\lambda_u + 2\mu)}$$

where p is the pore pressure, and r and t the distance from injection source and time, respectively; $\lambda_u = 2\mu\nu u/(1-2\nu_u)$ is the undrained Lamé parameter and the drained Lamé parameter without the subscript u; c is the hydraulic diffusivity which depends on permeability, k and viscosity, η. We account for poroelasticity of the medium in their effects on hydraulic transport, but ignore the poroelastic stresses themselves given that they are a small fraction of the stresses induced by pore pressure increase (Kim & Avouac, 2023; poroelastic parameters referred therein). Stress changes become input to the ODE formulation of Dieterich (1994), to solve for seismicity rate in space and time. The alternative integral formulation of Heimisson & Segall (2018) is used here as it is more tractable numerically for injection scenarios such as in Otaniemi and in Basel that consist of abrupt changes in the injection rate:

$$R(r,t) = \frac{K(r,t)}{1 + \frac{1}{t_a}\int_0^t K(r,t')dt'}$$

$$K(r,t) = exp\left(\frac{\tau(r,t)}{a\bar{\sigma}(r,t)} - \frac{\tau_0}{a\bar{\sigma_0}}\right)$$

$$t_a = \frac{a\bar{\sigma_0}}{\dot{\tau_r}}$$

$$\bar{\sigma} = \sigma - p$$

where r_b is the background seismicity rate, $\dot{\tau_r}$ the background stressing rate, a the rate-and-state friction parameter, σ the normal stress, σ_0 and τ_0 the initial normal and shear stress, and σ and τ the applied normal and shear stress, respectively. Synthetic catalogs are produced by sampling events from a non-homogeneous Poisson process using the acceptance-rejection method.

3.1 Seismicity rate modeling of Otaniemi stimulation

We invert for the hydraulic properties of the medium by matching the measured well-head pressure with the flow rates as input using the affine invariant Markov Chain Monte-Carlo (MCMC) Ensemble sampler of Goodman & Weare (2010). The best fit gives effective well radius and ambient pore pressure of 31m and 54.9MPa, respectively, and a diffusivity of 0.044 m^2/s (Figure 4). A similar approach is used to infer the parameters of the seismicity rate model, a, $\dot{\tau_r}$, and r_b from the time time history of the seismicity rate. In order to simplify the sampling process, the sampler computes the posterior of a and $\dot{\tau_r}$, and r_b - a multiplicative factor to the normalized seismicity rate - is subsequently adjusted for each pair of a and $\dot{\tau_r}$ to match the total number of observed events. The sampler conducts 2000 to 5000 iterations of 32 walkers. The prior is assumed to be uniform for both variables between the range of 10^{-5} to 10^{-2} and 0.1 kPa/yr. to 5 kPa/yr. for a and $\dot{\tau_r}$, respectively, although the shape of the prior is seen to have little effect on the posterior given the large sample size. The variation of injection locations between different stages in Otaniemi likely stimulated new volumes of rock. To this effect, we start a new simulation with the same initial conditions and compound the results for the final catalog. To test the ability of the model to act as a forecasting tool,

we infer the parameters of the seismicity rate model only from the seismicity history of the first injection stage. The best fitting model is then extrapolated for the rest of the injection period.

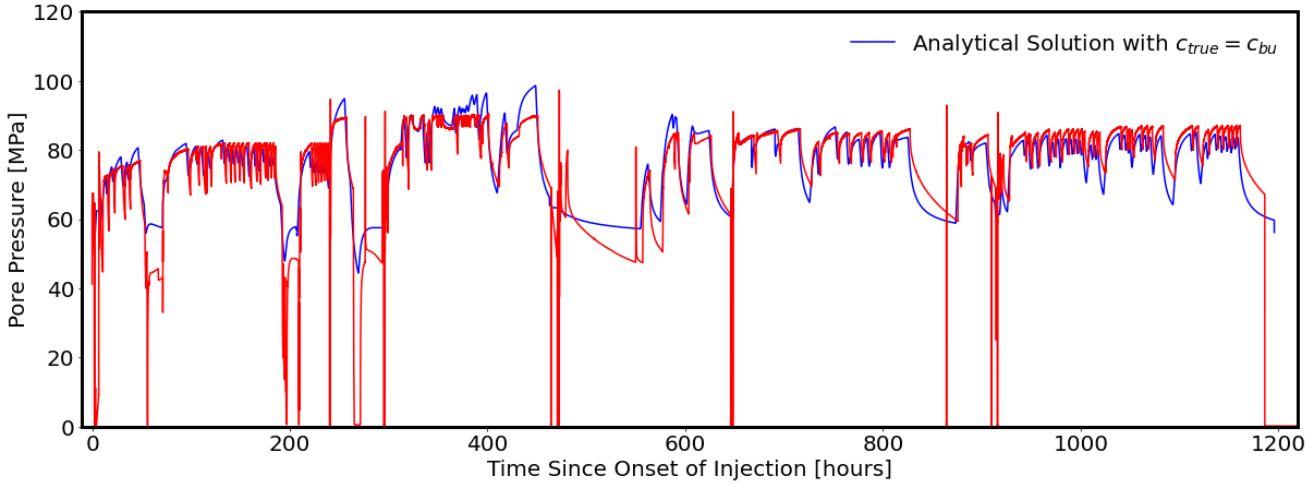

Figure 4: Measured and Modeled Well-head Pressure at Otaniemi: The measured well-head pressure in Otaniemi is plotted in red, and the best fitting pressure model (with c_{bu} = 0.044 m^2/s) is plotted in blue. The constant diffusivity model does a good job matching the rate of pressure build-up at the onset of injection cycles, but predicts significantly quicker relaxation to the background pressure level during shut-ins, indicating changes in the diffusivity due to the injections.

The resulting fit for the seismicity rate in time and space is shown in Figure 5. a, $\dot{\tau_r}$, and r_b of the best fit are 0.00005, 0.1kPa/year and 0.39 events/day, respectively. The model reproduces a good match to the observations, especially in the roughly direct correlation between the injection and seismicity rate along with the Omori law-like decay during shut-ins. The synthetic catalog in space also shows a good match with respect to the extent of the triggering front and cumulative distribution of events in space. The largest mismatch comes in the back-propagation fronts following shut-ins. It's possible that the back-propagation fronts are more strongly governed by a lower diffusivity as pressure decreases, leading to closing of fractures and hydraulic pathways. This coincides well with the observation that the rate of pressure drawdown during shut-ins is faster in the model (Figure 4).

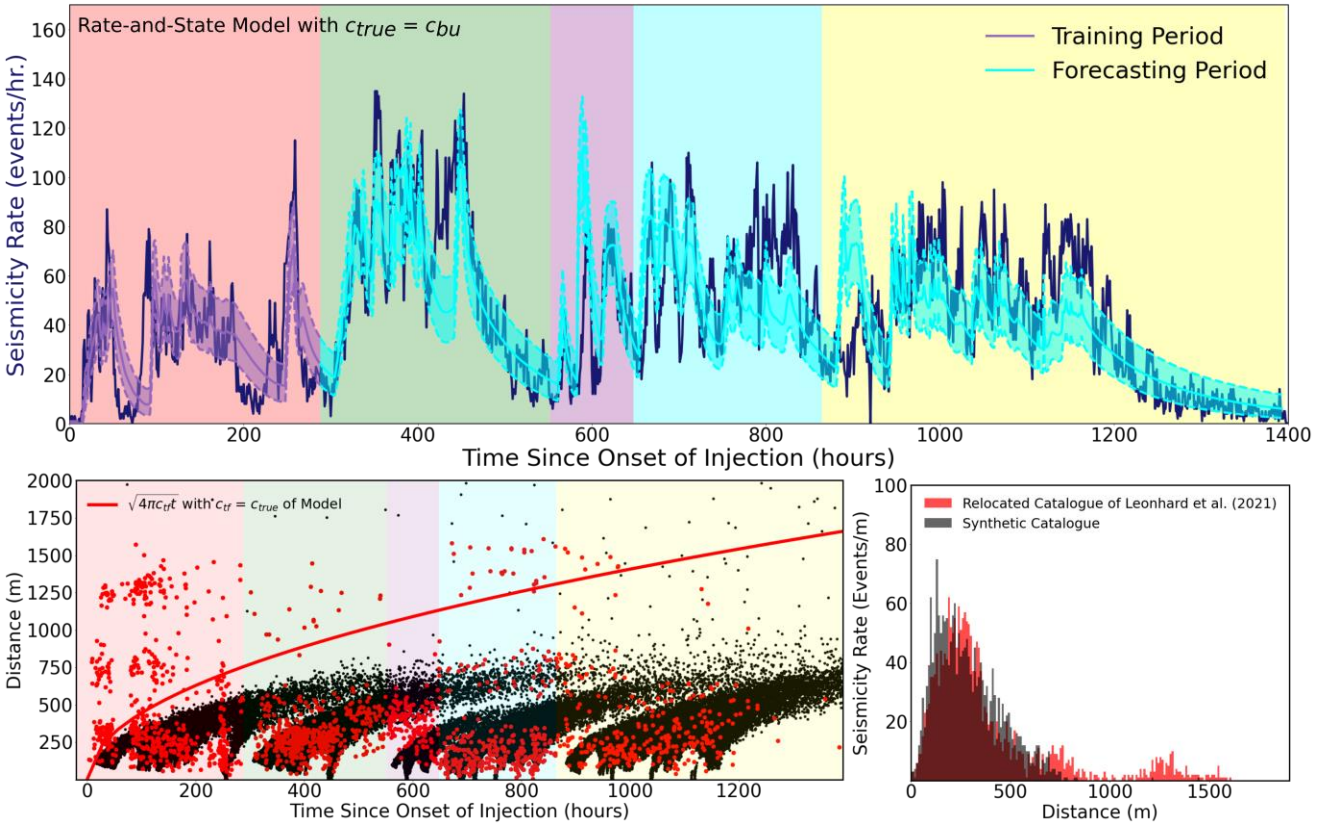

Figure 5: Pseudo-Forecast of Induced Seismicity in Otaniemi by Physical Modeling: The light purple shading shows the confidence interval of the model fit with parameters inferred from matching the observed seismicity rate during the first injection period. The light cyan shading shows the extrapolation of the model to the rest of the injection. The black dots of the synthetic catalog match well the distribution of the relocated events plotted in red.

We remark that the best fitting value of $a = 0.00005$ is significantly lower than the values inferred from laboratory measurements, generally ranging between 0.01 and 0.001 (Marone, 1998). One possible explanation is that spatial heterogeneities lead to elastic interactions that produce globally inferred values lower than that in a homogeneous equivalent (Dublanchet et al., 2013). It is also important to note that the model of Dieterich (1994) is a limited representation of the full complexity of rate-and-state friction. For example, the model simulates a population of spring-slider nucleation sources, whose qualitative differences in their behavior to more realistic finite fault models have been displayed for numerous aspects of rupture characteristics. Additionally, the model neglects the effect of variable effective normal stress on nucleation size, as the number of active nucleation sources remains constant throughout (Alghannam & Juanes, 2020). Further development of the model with a more holistic representation of rate-and-state friction would prove valuable for induced seismicity forecasting.

3.2 Seismicity rate modeling of Basel stimulation

We apply the same modeling framework developed for the Otaniemi stimulation in Section 3.1 to the Basel stimulation. One difficulty in modeling fluid transport in Basel is that the measured well-head pressure shows significantly greater nonlinearity with respect to the injection flow rate than in Otaniemi. The nonlinearity is easily evident when comparing the pressure increase due to increase in injection rate at the beginning to that towards the end of the injection schedule. The increments of rise in pressure become smaller with time (Gischig & Wiemer, 2013), likely indicating a significant increase in the diffusivity due to the creation of fractures and connection of the fault network. Furthermore, the relatively slow rate of pressure decrease at shut-in reflects a diffusivity significantly lower than the co-injection diffusivity (Gischig & Wiemer, 2013), likely due to the closing and healing of fractures. In order to account for the uncertainty introduced by what is likely a pressure-dependent diffusivity of the medium, fluid transport in Basel is not modeled using the injection rate but rather by enforcing the measured well-head pressure as a pressure boundary condition at the injection location. Then, we observe the sensitivity of the seismicity rate model parameters to a range of hydraulic diffusivity.

Example fits of the seismicity rate model to different diffusivities are shown in Figure 6. As discussed in Section 2.1, we also calibrate the model at different magnitudes of completeness to test the sensitivity to the different seismicity rate histories. A better fit overall to the time history of the seismicity rate is achieved at lower diffusivities, regardless of the magnitude of completeness. This is especially true to the rate of seismicity rate decay after shut-in. In all models with high diffusivity, the seismicity rate quickly decays to zero compared to the observations. At the same time, the heightened seismic response to injection rate changes are better modeled by higher diffusivities. This is consistent with how one would expect the diffusivity of the medium to change based on the injection rate. In Otaniemi, this effect was visible in the well-head pressure history. In Basel, this is evident both in the well-head pressure, and the seismicity rate evolution.

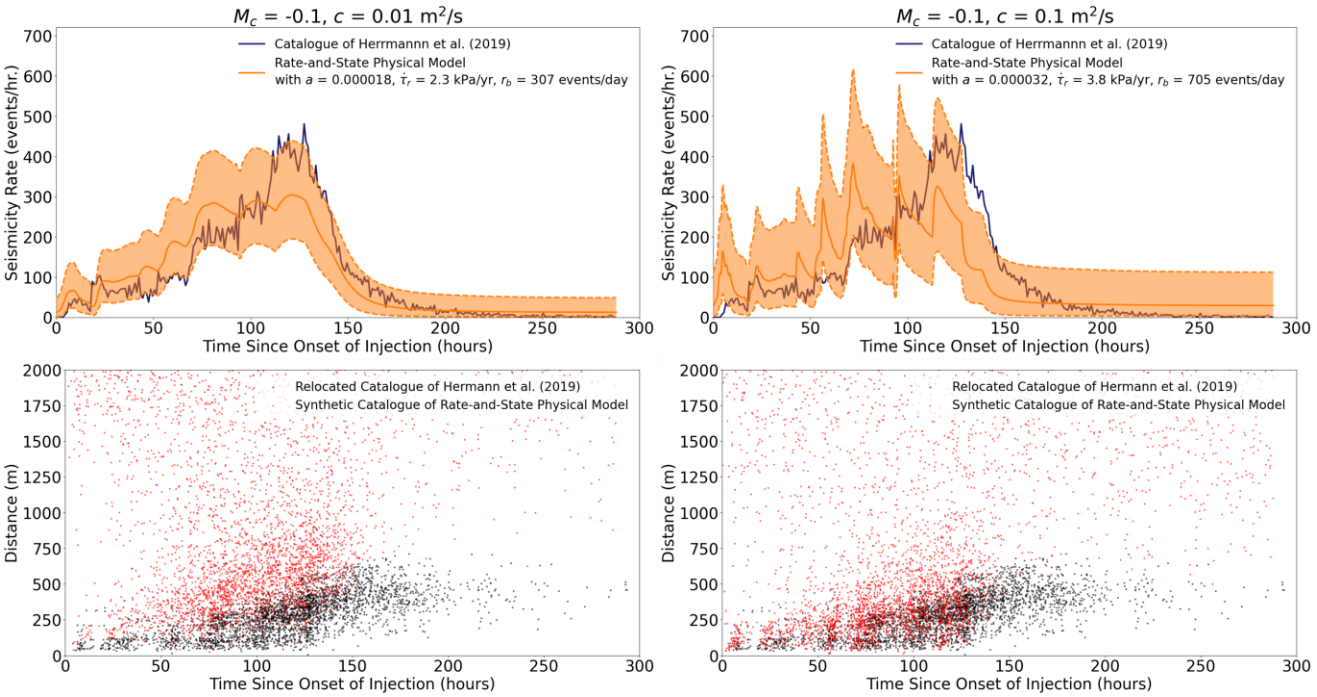

Figure 6: Seismicity Rate Modeling of Basel: The plot on the left shows the seismicity rate model that best fits the observations given a diffusivity of 0.01 m²/s and the right for a diffusivity of 0.1 m²/s. Both have magnitudes of completeness of -0.1. The model with lower diffusivity better matches the seismicity rate decay at shut-in while the model with higher diffusivity shows higher peaks at injection rate changes. In space (the bottom row) the model with higher diffusivity has a shorter reaching seismicity front like the observations (black) due to the higher value of *a*. Both models show a large proportion of events beyond the seismicity front due to the overestimated background seismicity rate.

The magnitude of completeness most strongly affects the background seismicity rate, r_b, such that r_b is higher at lower M_c to match the higher number of total events. For all models, r_b is significantly higher than intuitively expected, ranging between the orders of 100 to 10,000 events per day (Figure 7). This overestimate of r_b is evident when viewing the spatial profile of the synthetic catalogs where there is a significantly higher number of events beyond the main seismicity cloud compared to the relocated catalog. The spatial density of the main cluster is also best matched at higher diffusivity while the triggering front is overestimated at lower diffusivity. This occurs due to higher values of the seismicity rate parameter a from rate-and-state friction better matching the temporal history of the seismicity rate at higher diffusivities (Figure 7), and the product $a\sigma$ acting like a stress threshold that suppresses seismic events further away from the injection location (Kim & Avouac, 2023; Wenzel, 2017). The back-propagation front of the seismicity cloud, however, is overestimated at all diffusivities, with the cluster remaining closer to the injection location after shut-in in the relocated catalog. Such back-propagation fronts may be reproducible with a sudden decrease in diffusivity at shut-in, such that pressure changes propagate much more slowly due to healing of fractures.

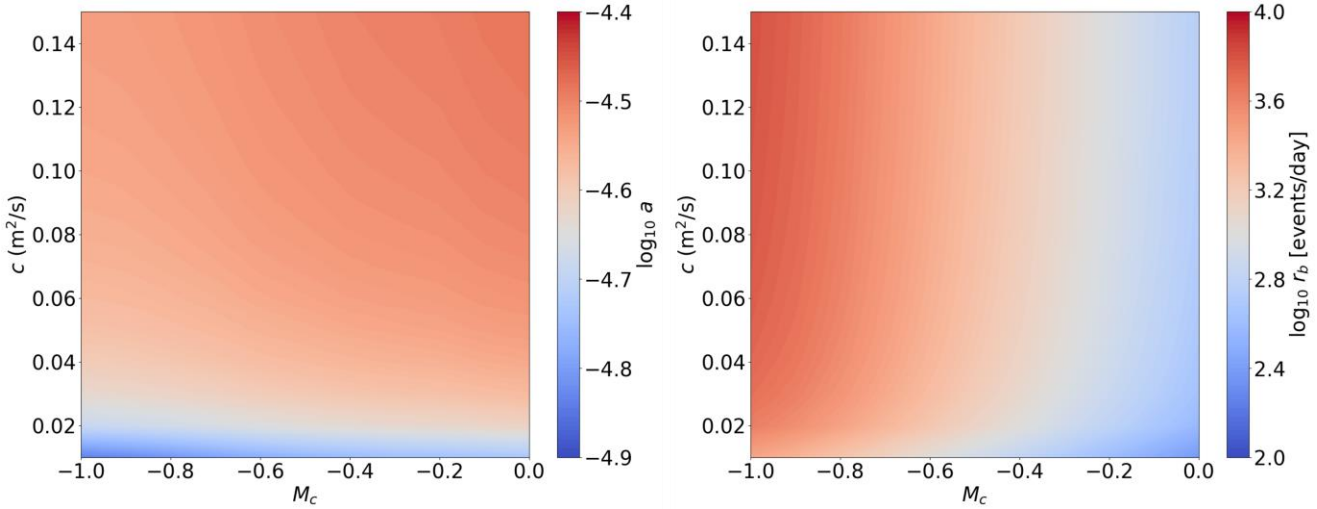

Figure 7: Sensitivity of Seismicity Rate Model Parameters to Magnitude of Completeness and Diffusivity: The contour plots show the parameters of the best fitting seismicity rate model given the diffusivity of the pressure model and the magnitude of completeness. The parameter *a* shows a strong dependence on the diffusivity, such that higher values of *a* are favored at

higher diffusivity. Due to higher values of a, models with higher diffusivity result in shorter reaching seismicity fronts. r_b shows the strongest dependence on M_c, such that it increases with decreasing M_c. r_b ranges between 100 to 10,000 events/day, likely an overestimate of the true value.

The significant overestimate of r_b in Basel raises the question of whether the variable indeed represents the intended physical meaning of the original Dieterich formulation when applied to injection settings. Specifically in the context of injection-induced seismicity, it's easy to imagine a scenario such that this would not be the case. Injections are often performed in historically non-tectonic areas in order to minimize the risk of earthquake hazard. If injections still induce earthquakes in this setting, the background seismicity rate of the Dieterich model would be an infinite overestimation of the true, near-zero value. What is more likely is that the seismicity rate response is sensitive to the initial conditions of the nucleation sources, which is assumed to be close to instability in the Dieterich model – a rather restrictive set of the parameter space. A numerical model that simulates frictional motions of nucleation sources individually with flexibility in the initial conditions would be necessary to investigate the exact meaning of the model's parameters in different applications.

4. SENSITIVITY OF INDUCED EARTHQUAKE MAGNITUDES TO DEPTH AND INJECTIONS

We study two variables commonly discussed in their influence on magnitudes in both natural and induced settings: depth and cumulative injected volume, V_{max}. First, we sort the events of the relocated catalogs by the variable in question and apply a moving window of a constant size (300 events). We estimate the b-value of each bin using the b-positive measure (van der Elst, 2021) for robustness to the choice of magnitude of completeness that may vary between each bin. The observed trends of each catalog are presented in the following.

4.1 Magnitude-frequency distribution in Otaniemi

Magnitude-Frequency distributions in Otaniemi show a dominant, negative correlation of the b-value with depth, (Figure 8) as is similarly observed in natural earthquakes. Plotting the magnitude-frequency distribution of all bins on top of each other shows remarkably well the shift of the distribution as well as a clear increase in the maximum magnitude, M_{max}, and M_c. The largest deviation from the linear decrease of the b-value with depth can be observed at about 6km near the average location of the injection, suggesting that stress changes due to the diffusion of fluids significantly affect the magnitude distribution. The apparent dependence of the magnitude-frequency distribution with depth must be considered with caution, however, as dependence of seismological observables on depth is associated with a large degree of uncertainty. For instance, either accounting for higher rupture velocity (Shearer, 2006; Allmann & Shearer, 2007) or weaker attenuation (Abercrombie et al., 2021) at greater depth can sufficiently explain the observed increase in stress drop. The significant increase in M_c with depth in Otaniemi may indicate such effects as smaller events go undetected further away from observation stations at much shallower depth.

In the interest of studying the relationship between the magnitudes and injections independently of such observational uncertainty, we apply a correction of the magnitudes that de-trends the variation of M_c and M_{max} with respect to depth. Once de-trended, the catalog shows a relatively weak dependence of the magnitude-frequency distribution on V_{max} while M_c and M_{max} increase with injected volume. The observation that M_{max} increases with V_{max} is qualitatively consistent with the assumption that ruptures may only extend to the edges of the stimulated volume (Shapiro et al., 2011). This effect predicts no changes to the size distribution of events smaller than M_{max}, consistent with the observed lack of a systematic variation of b-value with V_{max}. However, the variation of M_{max} is quantitatively different from what is expected by orders of magnitude. If assuming a constant stress drop of 1 MPa across a circular slip patch, the radius of the observed M_{max} event of 1.86 Mw would be 10.8 m. However, the stimulated volume as can be inferred from the seismicity cloud of the relocated catalog spans a significantly larger distance of more than 500m which would be more consistent with M_{max} events of ~4.6Mw. One possible explanation for the inconsistency is that M_{max} is also strongly dependent on fault connectivity where larger stimulated volumes allow slip to span across the total lengths of individual faults though none of which may span the entire stimulated volume.

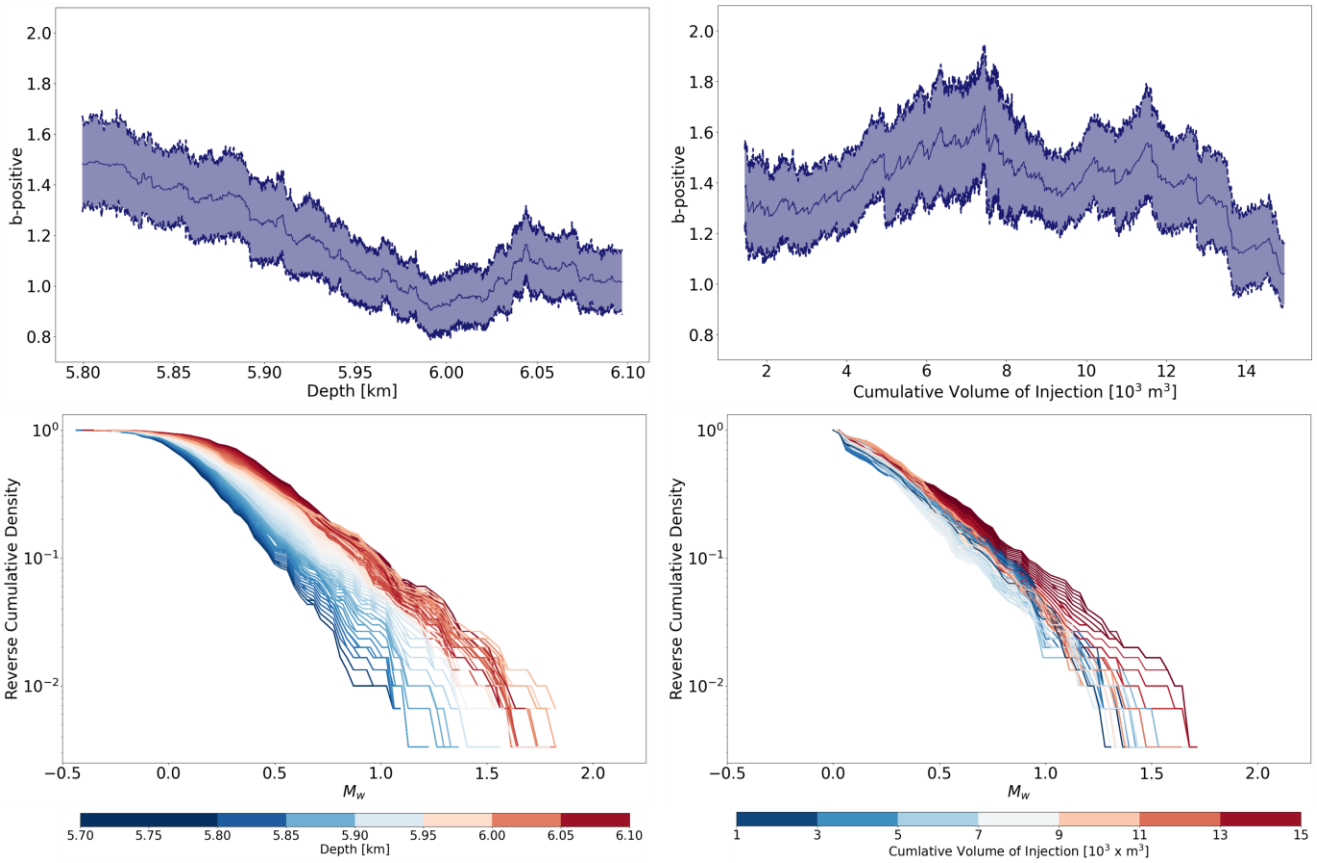

Figure 8: Sensitivity of Magnitudes to Depth and Injected Volume in Otaniemi: On the top row, earthquakes of the relocated catalog are sorted by depth and volume, and *b*-value's of the sorted bins are plotted along with a bootstrap estimate of the standard deviation. On the bottom row, the magnitude-frequency distribution of each bin is plotted with the color representing the sorting variable. The catalog shows a strong dependence of the *b*-value, M_{max}, and M_c to depth in Basel. After applying a depth-correction, M_{max}, and M_c are seen to increase with injected volume, while the *b*-value varies rather randomly.

4.2 Magnitude-frequency distribution in Basel

Unlike in Otaniemi, Basel does not show a clear trend of the magnitude-frequency distribution on depth (Figure 9), and no depth corrections are applied before observing the trend with respect to injections. The lack of a dependence on depth may be because depth-dependent attenuation effects are less pronounced in Basel. The dependence on cumulative injected volume is similar to that observed in Otaniemi such that the *b*-value varies randomly while M_{max} tends to be larger at greater injected volume. However, no obvious trends are observed for the variation of M_c.

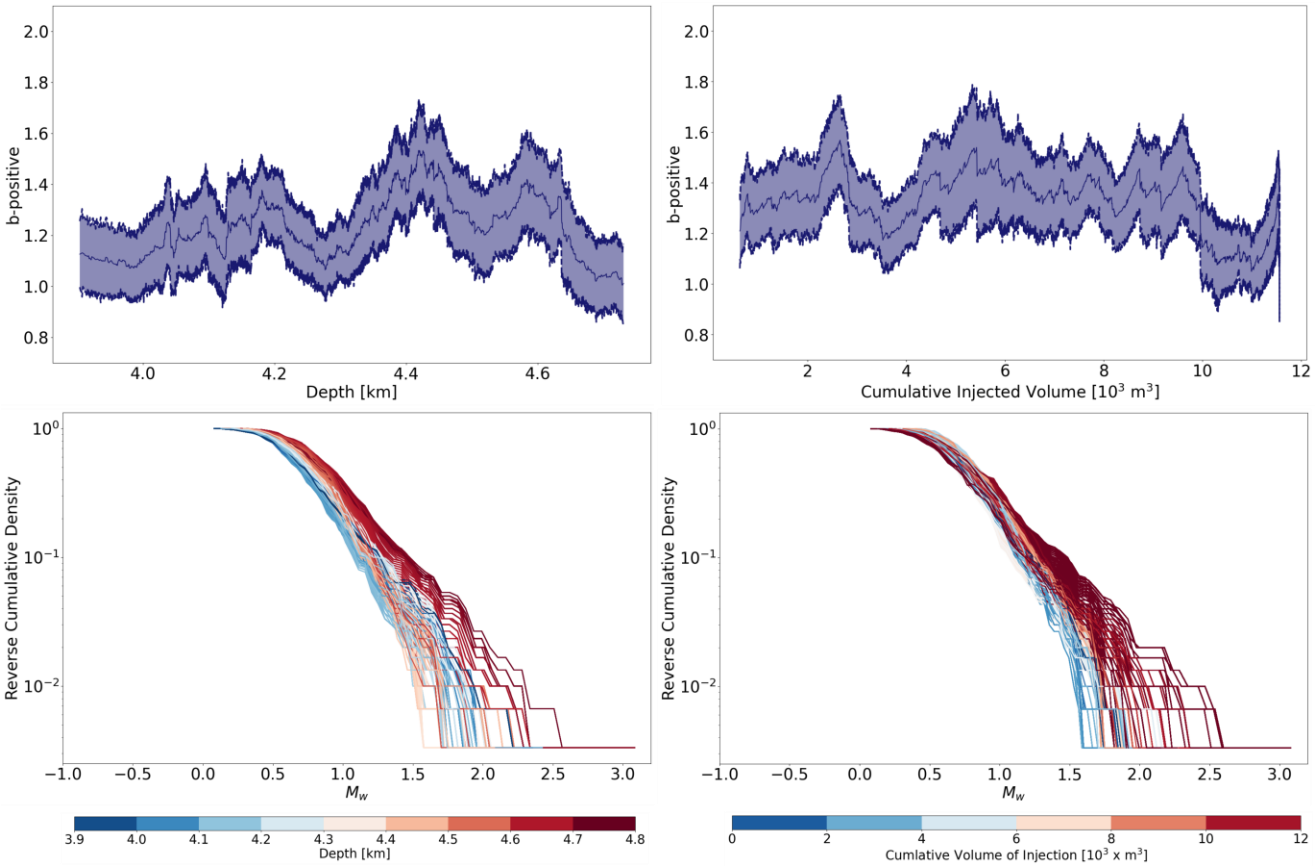

Figure 9: Sensitivity of Magnitudes to Depth and Injected Volume in Basel: On the top row, earthquakes of the relocated catalog are sorted by depth and volume, and *b*-value's of the sorted bins are plotted along with a bootstrap estimate of the standard deviation. On the bottom row, the magnitude-frequency distribution of each bin is plotted with the color representing the sorting variable. The Basel catalog shows no systematic correlation of magnitudes to depth. With no depth-correction, M_{max}, is seen to increase with injected volume, while the *b*-value and M_c varies randomly.

4.3 Dependence of magnitude-frequency distributions to distance from injection

The lack of a strong correlation between magnitudes and V_{max} may be attributed to its lack of spatial information about a single event that occurs at stress conditions varying in time and space. Analogously, characterization of events by depth misses temporal information about the earthquakes. Thus, sensitivity of magnitudes may be better captured by physical variables that account for spatiotemporal variations of the stress state such as pore pressure or pore pressure rate. Given the degree of uncertainty in the pressure models that do not account for evident changes in the diffusivity due to injections, we refrain from using the pressure model directly but rather sort the events by distance from the injection source as a proxy variable. The sensitivity of the magnitude-frequency distributions to distance from injection are shown in Figure 10.

Both catalogs show nonlinear trends such that the *b*-value initially increases with distance before decreasing. This trend was previously noted in Basel (Bachmann, et al., 2012), although the initial increase with distance near the injection source was regarded as a minor deviation from the main trend of decreasing *b*-value with distance. It is remarkable that the initial increase in *b*-value is also visible in Otaniemi, and the distance at which *b*-value begins to decrease is similar, at around 200-250m. One possibility is that the location at which the *b*-value trend switches marks the boundaries of regions with different dominant stress mechanisms. One would expect that near the injection source, the dominant mechanism of earthquake triggering would be effective stress decrease by fluid pressurization, whereas poroelastic stresses or elastic stress transfer from seismic/aseismic slip caused by other earthquakes may become more prevalent further away. In fact, previous studies indicate that Coulomb stress changes in Basel can be expected to increase with distance (Catalli et al., 2013), and that source to source interactions in Basel may account for a significant portion of the total observed seismicity (Catalli et al., 2016). In order to comprehensively interpret the nonlinear trend of the *b*-value with respect to distance, one may need to differentiate triggering mechanisms and take into account the initial stress threshold of the individual nucleation sources.

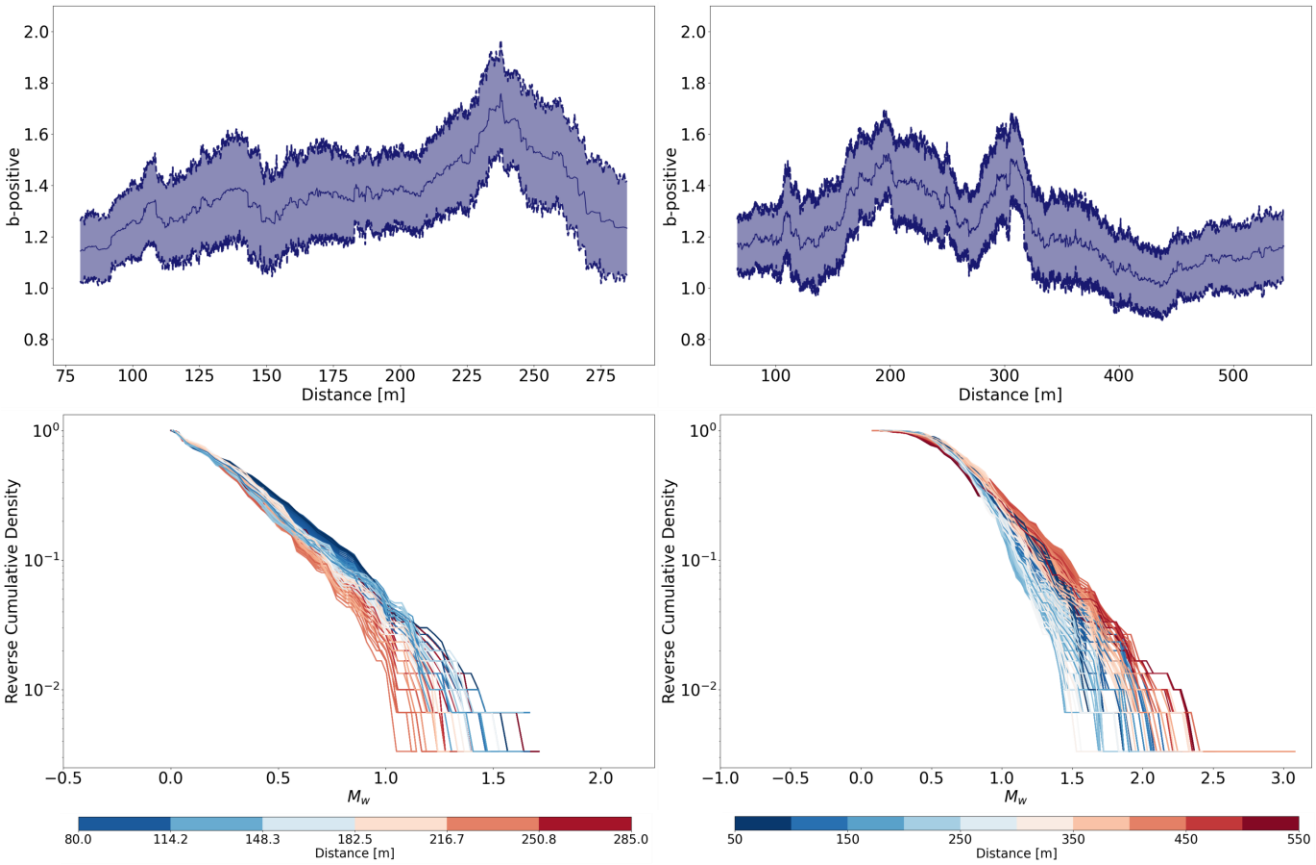

Figure 10: Sensitivity of Magnitudes to Distance from Injection in Otaniemi (left; with depth correction) and Basel (right; without depth correction): Both catalogs show an initially increasing *b*-value with increasing distance, before the *b*-value starts to drop at around 200 -250m.

5. CONCLUSIONS

The modeling methods presented here could be useful in designing EGS operations or to interpret induced seismicity observations in terms of transport properties within the stimulated volume. They could additionally serve as a basis for a probabilistic traffic light system (TLS) or be incorporated in a control and optimization framework (Stefanou, 2019). At the moment, TLS are deterministic and based entirely on the observed maximum magnitude (Ader et al. 2020; Bommer et al. 2006; Kwiatek et al., 2019; Majer et al. 2007). The observed dependence of induced earthquake magnitudes on depth and injections has significant implications on the challenges facing enhanced geothermal stimulation. Enhanced geothermal stimulation often seeks extraction from unconventional thermal reservoirs at unusually great depth. Both the observed increase in M_{max} and decrease in *b*-value with depth would suggest that such operations would inevitably encounter higher chances of larger events. Thus, the a key feature that accompany most EGS operations may be a driving mechanism for triggering red-light events. The lack of a depth-dependence in Basel suggests that the observation in Otaniemi could be an artificial effect of depth-dependent attenuation. In such a case, it will be important to identify the cause for the *b*-value relationship with respect to distance. Proper identification of the physical mechanism governing induced earthquake magnitudes could pose a threshold probability of a red-light event as a constraint. Given the urgency of clean energy solutions, further observations of the relationship between induced magnitudes and the local stress changes, in addition to numerical models of induced seismicity that take into account different initial stability conditions could be immensely valuable.

REFERENCES <HEADING 1 STYLE>

Abercrombie, R. E., Trugman, D. T., Shearer, P. M., Chen, X., Zhang, J., Pennington, C. N., ... & Ruhl, C. J. (2021). Does earthquake stress drop increase with depth in the crust?. Journal of Geophysical Research: Solid Earth, 126(10), e2021JB022314.

Ader, T. J., Chendorain, M., Free, M., Saarno, T., Heikkinen, P., Malin, P. E., et al. (2020). Design and implementation of a traffic light system for deep geothermal well stimulation in Finland. Journal of Seismology, 24(5), 991–1014.

Aki, K., Fehler, M., Aamodt, R. L., Albright, J. N., Potter, R. M., Pearson, C. M., & Tester, J. W. (1982). Interpretation of seismic data from hydraulic fracturing experiments at the Fenton Hill, New Mexico, hot dry rock geothermal site. Journal of Geophysical Research: Solid Earth, 87(B2), 936–944.

Alghannam, M., & Juanes, R. (2020). Understanding rate effects in injection-induced earthquakes. Nature Communications, 11(1), 1–6.

Allmann, B. P., & Shearer, P. M. (2007). Spatial and temporal stress drop variations in small earthquakes near Parkfield, California. Journal of Geophysical Research, 112, B04305.

Bachmann, C. E., Wiemer, S., Goertz-Allmann, B. P., & Woessner, J. (2012). Influence of pore-pressure on the event-size distribution of induced earthquakes. Geophysical Research Letters, 39(9).

Bommer, J. J., Oates, S., Cepeda, J. M., Lindholm, C., Bird, J., Torres, R., & Rivas, J. (2006). Control of hazard due to seismicity induced by a hot fractured rock geothermal project. Engineering Geology, 83(4), 287–306.

Catalli, F., Meier, M. A., & Wiemer, S. (2013). The role of Coulomb stress changes for injection-induced seismicity: The Basel enhanced geothermal system. Geophysical Research Letters, 40(1), 72-77.

Catalli, F., Rinaldi, A. P., Gischig, V., Nespoli, M., & Wiemer, S. (2016). The importance of earthquake interactions for injection-induced seismicity: Retrospective modeling of the Basel Enhanced Geothermal System. Geophysical Research Letters, 43(10), 4992-4999.

Dieterich, J. H. (1994). A constitutive law for rate of earthquake production and its application to earthquake clustering. Journal of Geophysical Research: Solid Earth, 99(B2), 2601–2618.

Dieterich, J. H., & Linker, M. F. (1992). Fault stability under conditions of variable normal stress. Geophysical Research Letters, 19(16), 1691–1694.

Dublanchet, P. (2018). The dynamics of earthquake precursors controlled by effective friction. Geophysical Journal International, 212(2), 853–871.

Elmar, E., & Shapiro, S. A. (2002). Microseismic monitoring of borehole fluid injections: Data modeling and inversion for hydraulic properties of rocks. OnePetro.

Elsworth, D., Spiers, C. J., & Niemeijer, A. R. (2016). Understanding induced seismicity. Science, 354(6318), 1380–1381.

Gaucher, E., Schoenball, M., Heidbach, O., Zang, A., Fokker, P. A., van Wees, J. D., & Kohl, T. (2015). Induced seismicity in geothermal reservoirs: A review of forecasting approaches. Renewable and Sustainable Energy Reviews, 52, 1473–1490.

Gischig, V. S., & Wiemer, S. (2013). A stochastic model for induced seismicity based on non-linear pressure diffusion and irreversible permeability enhancement. Geophysical Journal International, 194(2), 1229-1249.

Goodman, J., & Weare, J. (2010). Ensemble samplers with affine invariance. Communications in Applied Mathematics and Computational Science, 5(1), 65–80.

Grigoli, F., Cesca, S., Priolo, E., Rinaldi, A. P., Clinton, J. F., Stabile, T. A., et al. (2017). Current challenges in monitoring, discrimination, and management of induced seismicity related to underground industrial activities: A European perspective. Reviews of Geophysics, 55(2), 310–340.

Gulia, L., & Wiemer, S. (2010). The influence of tectonic regimes on the earthquake size distribution: A case study for Italy. Geophysical Research Letters, 37(10).

Häring, M. O., Schanz, U., Ladner, F., & Dyer, B. C. (2008). Characterisation of the Basel 1 enhanced geothermal system. Geothermics, 37(5), 469-495.

Healy, J. H., Rubey, W. W., Griggs, D. T., & Raleigh, C. B. (1968). The Denver earthquakes. Science, 161(3848), 1301–1310.

Heimisson, E. R., & Segall, P. (2018). Constitutive law for earthquake production based on rate-and-state friction: Dieterich 1994 revisited. Journal of Geophysical Research: Solid Earth, 123(5), 4141–4156.

Herrmann, M., Kraft, T., Tormann, T., Scarabello, L., & Wiemer, S. (2019). A consistent high-resolution catalog of induced seismicity in Basel based on matched filter detection and tailored post-processing. Journal of Geophysical Research: Solid Earth, 124(8), 8449-8477.

Hillers, G., Vuorinen, T. A. T., Uski, M. R., Kortström, J. T., Mäntyniemi, P. B., Tiira, T., et al. (2020). The 2018 geothermal reservoir stimulation in Espoo/Helsinki, southern Finland: Seismic network anatomy and data features. Seismological Research Letters, 91(2), 770–786.

Kim, T., & Avouac, J. P. (2023). Stress-Based and Convolutional Forecasting of Injection-Induced Seismicity: Application to the Otaniemi Geothermal Reservoir Stimulation. Journal of Geophysical Research: Solid Earth, 128(4), e2022JB024960.

Kwiatek, G., Saarno, T., Ader, T., Bluemle, F., Bohnhoff, M., Chendorain, M., et al. (2019). Controlling fluid-induced seismicity during a 6.1 km deep geothermal stimulation in Finland. Science Advances, 5, 5.

Leonhardt, M., Kwiatek, G., Martínez-Garzón, P., Bohnhoff, M., Saarno, T., Heikkinen, P., & Dresen, G. (2021). Seismicity during and after stimulation of a 6.1 km deep enhanced geothermal system in Helsinki, Finland. Solid Earth, 12(3), 581–594.

Majer, E. L., Baria, R., Stark, M., Oates, S., Bommer, J., Smith, B., & Asanuma, H. (2007). Induced seismicity associated with enhanced geother-mal systems. Geothermics, 36(3), 185–222.

Marone, C. (1998). The effect of loading rate on static friction and the rate of fault healing during the earthquake cycle. Nature, 391(6662), 69–72.

McGarr, A. (2014). Maximum magnitude earthquakes induced by fluid injection. Journal of Geophysical Research: solid earth, 119(2), 1008-1019.

Mori, J., & Abercrombie, R. E. (1997). Depth dependence of earthquake frequency-magnitude distributions in California: Implications for rupture initiation. Journal of Geophysical Research: Solid Earth, 102(B7), 15081-15090.

Raleigh, C. B., Healy, J. H., & Bredehoeft, J. D. (1976). An experiment in earthquake control at Rangely, Colorado. Science, 191(4233), 1230–1237.

Rudnicki, J. W. (1986). Fluid mass sources and point forces in linear elastic diffusive solids. Mechanics of Materials, 5(4), 383–393.

Ruina, A. (1983). Slip instability and state variable friction laws. Journal of Geophysical Research: Solid Earth, 88(B12), 10359–10370.

Scholz, C. H. (2015). On the stress dependence of the earthquake b value. Geophysical Research Letters, 42(5), 1399-1402.

Schorlemmer, D., Wiemer, S., & Wyss, M. (2005). Variations in earthquake-size distribution across different stress regimes. Nature, 437(7058), 539-542.

Schultz, R., Skoumal, R. J., Brudzinski, M. R., Eaton, D., Baptie, B., & Ellsworth, W. (2020). Hydraulic fracturing-induced seismicity. Reviews of Geophysics, 58, 3.

Segall, P., & Lu, S. (2015). Injection-induced seismicity: Poroelastic and earthquake nucleation effects. Journal of Geophysical Research: Solid Earth, 120(7), 5082–5103.4

Shapiro, S. A., Audigane, P., & Royer, J. J. (1999). Large-scale in situ permeability tensor of rocks from induced microseismicity. Geophysical Journal International, 137(1), 207–213.

Shapiro, S. A., Dinske, C., & Rothert, E. (2006). Hydraulic-fracturing controlled dynamics of microseismic clouds. Geophysical Research Letters, 33, 14.

Shapiro, S. A., Huenges, E., & Borm, G. (1997). Estimating the crust permeability from fluid-injection-induced seismic emission at the KTB site. Geophysical Journal International, 131(2), F15–F18.

Shapiro, S. A., Krüger, O. S., Dinske, C., & Langenbruch, C. (2011). Magnitudes of induced earthquakes and geometric scales of fluid-stimulated rock volumes. Geophysics, 76(6), WC55-WC63.

Shapiro, S. A., Rothert, E., Rath, V., & Rindschwentner, J. (2002). Characterization of fluid transport properties of reservoirs using induced microseismicity. Geophysics, 67(1), 212–220.

Shearer, P. M., Prieto, G. A., & Hauksson, E. (2006). Comprehensive analysis of earthquake source spectra in Southern California. Journal of Geophysical Research, 111, B06303.

Skempton, A. (1984). Effective stress in soils, concrete, and rocks. Selected Papers on Soil Mechanics, 1032, 4–16.

Spada, M., Tormann, T., Wiemer, S., & Enescu, B. (2013). Generic dependence of the frequency-size distribution of earthquakes on depth and its relation to the strength profile of the crust. Geophysical research letters, 40(4), 709-714.

Stefanou, I. (2019). Controlling anthropogenic and natural seismicity: Insights from active stabilization of the spring-slider model. Journal of Geophysical Research: Solid Earth, 124(8), 8786–8802.

van der Elst, N. J. (2021). B-positive: A robust estimator of aftershock magnitude distribution in transiently incomplete catalogs. Journal of Geophysical Research: Solid Earth, 126(2), e2020JB021027.

van der Elst, N. J., Page, M. T., Weiser, D. A., Goebel, T. H., & Hosseini, S. M. (2016). Induced earthquake magnitudes are as large as (statistically) expected. Journal of Geophysical Research: Solid Earth, 121(6), 4575-4590.

Wenzel, F. (2017). Fluid-induced seismicity: Comparison of rate-and state-and critical pressure theory. Geothermal Energy, 5(1), 1–16.

Zang, A., Oye, V., Jousset, P., Deichmann, N., Gritto, R., McGarr, A., & Bruhn, D. (2014). Analysis of induced seismicity in geothermal reservoirs—An overview. Geothermics, 52, 6–21.

Zhai, G., & Shirazei, M. (2018). Fluid injection and time-dependent seismic hazard in the Barnett shale, Texas. Geophysical Research Letters, 45(10), 4743–4753.